











RESEARCH ARTICLE | MARCH 26 2025

Strain evolution in $\text{La}_{0.6}\text{Sr}_{0.4}\text{CoO}_{3-\delta}$ and $\text{SrTi}_{0.3}\text{Fe}_{0.7}\text{O}_{3-\delta}$ multilayer systems

Sergej Ražnjević ; Sandra Drev ; Andreas E. Bumberger ; Matthäus Siebenhofer ; Christin Böhme ; Christoph Riedl; Jürgen Fleig ; Miran Čeh ; Markus Kubicek ; Zaoli Zhang  



J. Appl. Phys. 137, 125304 (2025)

<https://doi.org/10.1063/5.0250573>



View Online



Export Citation

Articles You May Be Interested In

Electron beam-induced brownmillerite–perovskite phase transition in $\text{La}_{0.6}\text{Sr}_{0.4}\text{CoO}_{3-\delta}$

Appl. Phys. Lett. (May 2023)

The effect of Eu substitution on thermoelectric properties of $\text{SrTi}_{0.8}\text{Nb}_{0.2}\text{O}_3$

J. Appl. Phys. (December 2007)

Structural properties of slightly off-stoichiometric homoepitaxial $\text{SrTi}_{x}\text{O}_{3-\delta}$ thin films

J. Appl. Phys. (August 2000)



Journal of Applied Physics

Special Topics Open
for Submissions

[Learn More](#)

Strain evolution in $\text{La}_{0.6}\text{Sr}_{0.4}\text{CoO}_{3-\delta}$ and $\text{SrTi}_{0.3}\text{Fe}_{0.7}\text{O}_{3-\delta}$ multilayer systems

Cite as: J. Appl. Phys. 137, 125304 (2025); doi: 10.1063/5.0250573

Submitted: 26 November 2024 · Accepted: 2 March 2025 ·

Published Online: 26 March 2025



Sergej Ražnjević,¹ Sandra Drev,² Andreas E. Bumberger,³ Matthäus Siebenhofer,^{3,4} Christin Böhme,³ Christoph Riedl,³ Jürgen Fleig,³ Miran Čeh,² Markus Kubicek,³ and Zaoli Zhang^{1,a)}

AFFILIATIONS

¹Erich Schmid Institute of Materials Science, Austrian Academy of Sciences, Jahnstraße 12, Leoben 8700, Austria

²Center for Electron Microscopy and Microanalysis, Jožef Stefan Institute, Jamova cesta 39, Ljubljana 1000, Slovenia

³Institute of Chemical Technologies and Analytics, TU Wien, Getreidemarkt 9, Vienna A-1060, Austria

⁴Department of Nuclear Science and Engineering, Massachusetts Institute of Technology, 77 Massachusetts Avenue, Cambridge, Massachusetts 02141, USA

^{a)}Author to whom correspondence should be addressed: zaoli.zhang@oeaw.ac.at

ABSTRACT

In this work, we investigated $\text{La}_{0.6}\text{Sr}_{0.4}\text{CoO}_{3-\delta}$ / $\text{SrTi}_{0.3}\text{Fe}_{0.7}\text{O}_{3-\delta}$ multilayer systems with different layer thicknesses. Reciprocal space mapping showed splitting of the reflections in the sample with 5 nm layers while for 15 nm thick layers reflections have been elongated. Using transmission electron microscopy, we investigated this phenomenon at the atomic scale and showed that the alternating 15 nm layers gradually increase their tensile out-of-plane strain, whereas the sample with 5 nm layers maintains a relatively stable strain state. In-plane strain relaxation is similar in both samples. Still, it differs in the strain relaxation mechanism, which involves the formation of amorphous regions in the 5 nm sample and the formation of edge dislocations in the 15 nm sample. Electron energy loss spectroscopy was employed to probe the oxidation states of Co, Fe, and Ti. In both samples, the oxygen vacancy concentration increases toward the surface.

© 2025 Author(s). All article content, except where otherwise noted, is licensed under a Creative Commons Attribution-NonCommercial 4.0 International (CC BY-NC) license (<https://creativecommons.org/licenses/by-nc/4.0/>). <https://doi.org/10.1063/5.0250573>

I. INTRODUCTION

Due to the huge CO_2 footprint of modern society, solid oxide fuel cells (SOFC's) are being widely investigated because they are a promising candidate to be used for CO_2 -emission free energy conversion.¹ However, for most materials, the high operating temperatures (≈ 700 – 1000 °C) limits their potential for commercial use.^{2–5} Therefore, lowering the operating temperatures of SOFCs, to the intermediate level of about 500–700 °C, has become one of the main tasks.⁶

A promising approach to overcoming these temperature challenges involves the use of multilayer systems which have been widely investigated in the past decade because of their potential to enhance existing technology and to help develop new ones.⁷ They are fabricated by depositing two or more different materials on top of each other in an alternating fashion. Growing multilayer samples implies the existence of many heterointerfaces between the layers. Those heterointerfaces between two different materials can produce

new properties that neither of the two materials initially have.⁸ For example, due to the epitaxial strain, strontium-doped lanthanum cobaltite (LSC) may undergo oxygen vacancy ordering, which can lead to the phase change from perovskite to brownmillerite.^{9–11} Additionally, LSC material is highly sensitive to the oxygen vacancy concentration, which can alter its crystal and electronic structure, as well as its magnetic properties.^{12,13}

LSC is one of the most promising perovskites for SOFC's usage as the cathode electrode because it is able to operate in the intermediate temperature range.^{5,14–18} Because most of the perovskites can be stabilized on a SrTiO_3 (STO) substrate, it makes STO the most used substrate material for perovskite investigation.¹⁹ The incorporation of Fe atoms into the STO matrix induces the formation of oxygen vacancies to compensate for the charge imbalance resulting from the mixed valence state of $\text{Fe}^{3+}/\text{Fe}^{4+}$.²⁰ It has been shown that highly Fe-doped STO (STF) is a good mixed conductor and that the electrical conducting character increases with the

03 June 2025 08:16:09

Fe-doping.^{20–22} Combining those two, LSC and STF, in multilayers may lead to novel improved properties.

In this work, we investigated strain evolution of multilayer samples made of $\text{La}_{0.6}\text{Sr}_{0.4}\text{CoO}_{3-\delta}$ (LSC) and $\text{SrTi}_{0.3}\text{Fe}_{0.7}\text{O}_{3-\delta}$ (STF) with different layers thicknesses of 5 nm in one and 15 nm in the other sample. Due to the lattice mismatch between the STF ($a = 3.886 \text{ \AA}$)²³ and LSC ($a = 3.838 \text{ \AA}$)²⁴ tensile strain is expected to be imposed in the LSC layers while compressive strain is expected in the STF layers. Furthermore, the whole system is further tensile strained from the buffer layer deposited on a substrate. Comparing samples with different sample thicknesses allows for examining strain relaxation differences and the behavior of oxygen atoms and vacancies across the layers.

II. EXPERIMENTAL PROCEDURE

In this work, two multilayer samples were deposited consisting of layers $\text{La}_{0.6}\text{Sr}_{0.4}\text{CoO}_{3-\delta}$ (LSC) and $\text{SrTi}_{0.3}\text{Fe}_{0.7}\text{O}_{3-\delta}$ (STF) with different thicknesses and we will refer to them as a “thick” and “thin” sample, respectively. These multilayer systems were deposited on yttria-stabilized zirconia (YSZ) single crystal with a buffer layer of $\text{Ce}_{0.8}\text{Gd}_{0.2}\text{O}_{2-\delta}$ (GDC). The YSZ substrates were obtained from Crystec GmbH and prepared through a thorough cleaning process to eliminate any polishing residues. This involved sequential sonication in ethanol for 30 min, followed by two cycles in 3% Extran® MA 02 (Merck) for 30 min each, and a final rinse in distilled water for 15 min. After cleaning, the substrates were annealed in a tube furnace at 1350 °C for 6 h in air, resulting in atomically flat YSZ surfaces. Figure 1(a) shows a schematic 3D model of the samples. From Fig. 1(a), the rotation relationship between the GDC buffer layer and the multilayer system can be seen. The atomistic scale model of this rotation relationship is shown in Fig. 1(b). Both samples were deposited using the pulsed laser deposition (PLD) technique. In the thick sample, 35 nm of epitaxial LSC-0 was grown on a (100) YSZ single

crystal with a 15 nm GDC buffer layer. Then, on the LSC-0 layer, we deposited three alternating layers of STF and LSC (labeled as STF-1,2,3 and LSC-1,2,3 respectively), all having a thickness of about 15 nm. The thin sample was deposited similarly, but here, the GDC buffer layer has a thickness of about 5 nm while the LSC-0 layer has a thickness of about 35 nm. Then, three 5 nm thick, alternating layers of the STF and LSC were deposited on top of the 35 nm LSC-0 layer. The total thickness of the thick sample is around 140 nm, while the total thickness of the thin sample is around 70 nm. In the thick sample, the GDC buffer layer was deposited in a 0.01 mbar O_2 atmosphere and the subsequent LSC and STF layers were deposited in a 0.04 mbar O_2 atmosphere. All layers, including GDC, in a thin sample were deposited in a 0.04 mbar O_2 atmosphere. During both deposition processes, a laser frequency of 1 Hz was used and the deposition was carried out at 600 °C.

For both samples, the orientation relationship between the substrate and the buffer layer is $(010)_{\text{YSZ}} \parallel (010)_{\text{GDC}}$ and $[010]_{\text{YSZ}} \parallel [010]_{\text{GDC}}$ while the LSC-0 layer exhibits a 45° in-plane rotation with respect to the GDC, giving a relation of $(010)_{\text{GDC}} \parallel (01-1)_{\text{LSCO}}$ and $[010]_{\text{GDC}} \parallel [01-1]_{\text{LSCO}}$. This orientation relationship is showcased in Fig. 1(b). The alternating multilayer system has the same orientation as the first LSC-0 layer.

X-ray diffractometry (XRD) analysis was conducted using a Malvern–Panalytical Empyrean x-ray diffractometer, which is equipped with a GaliPIX3D detector and a hybrid monochromator.

To examine the multilayer system on a transmission electron microscope, we prepared samples by employing a focused ion beam (FIB) technique with a Thermo Fisher Scios 2 DualBeam FIB/SEM. The Ga-ion beam was initially operated at 30 kV for material removal. To minimize damage to the crystal structure, the final stages of sample preparation involved reducing the accelerating voltage to 5 kV, followed by a final polish at 2 kV.

The atomic structure was systematically investigated using a JEOL ARM200F microscope equipped with a probe corrector and a

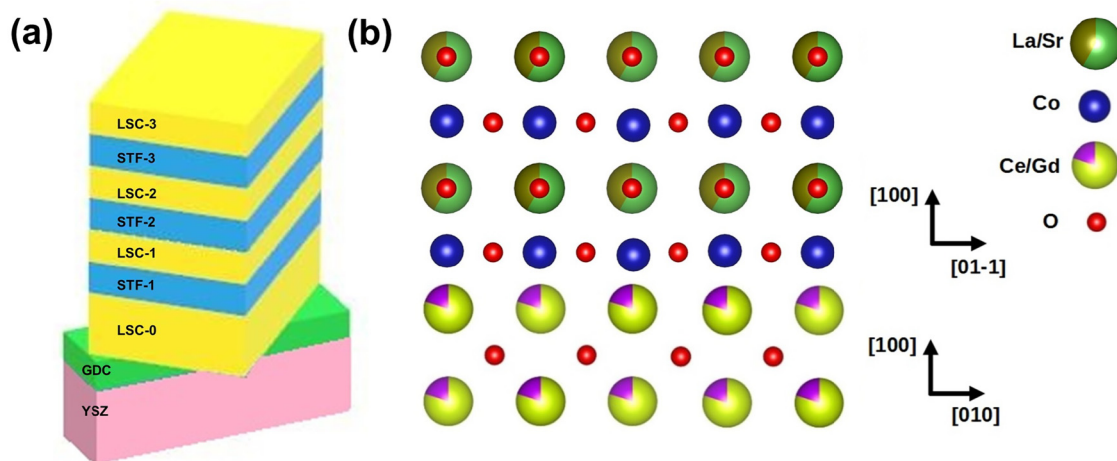


FIG. 1. (a) presents a schematic model of the multilayer systems. (b) is the interface model between the GDC buffer layer and the LSC layer which grows 45° rotation relative to the GDC layer.

03 June 2025 08:16:09

JEOL 2100F microscope equipped with an image-side Cs-corrector. High-angle annular dark field (HAADF) micrographs were obtained with a 68–280 mrad collection semi-angle range. Recorded images were denoised using the nonlinear (NL) filtering algorithm.²⁵ In order to examine the local strain relaxation, we apply the geometrical phase analysis (GPA) technique.²⁶

Electron energy loss spectroscopy (EELS) was employed via spot measurement on a Jeol ARM200F, equipped with a dual EELS Quantum spectrum-imaging filter, for a thick sample. EELS investigations of the thin sample were performed via the line-scan method on a Jeol 2100F which is equipped with a tridien system. The collection and convergence semi-angles were set to 125 and 7.5 mrad, respectively, with a dispersion of 0.3 eV per channel. The energy resolution was specified at 1.5 eV. Signal filtration was performed using principal component analysis (PCA), an integrated feature provided within the Gatan Microscopy Suite. The white-line ratio was calculated utilizing the Pearson model.^{27–30} In this approach, we integrate the area under the L₂ and L₃ peaks while employing a step function to eliminate the background. The height ratio of these steps is intentionally set at 2:1 to precisely reflect the 2p spin-orbit split states.

The quantification of the oxygen pre-peak involved integrating the intensity within a specific energy range. This method entailed fitting a Gaussian function to the oxygen pre-peak of both thin and thick samples' LSC-0 layers. The integration range for all layers was determined by the full-width-half maximum (FWHM) of the corresponding LSC-0 layer (see Fig. S1 in the [supplementary material](#)). Due to the sample thickness decrease toward the surface, the background was taken from the noise area (from raw data) just before the O K-edge onset. Relative noise intensity ratio was determined and from these measurements, intensity signals of the thin sample oxygen pre-peak were increased by 9.72%, 17.46%, and 31.73% for LSC-1, LSC-2, and LSC-3 layers, respectively.

III. RESULTS AND DISCUSSION

To achieve epitaxial growth of the multilayer system, it is imperative to deposit a GDC buffer layer to accommodate the

substantial lattice mismatch between YSZ and the LSC-STF system.³¹ Figure 2 illustrates the interface between the YSZ substrate and the GDC buffer layer, accompanied by their respective in-plane phase images. The phase images distinctly reveal the presence of misfit dislocations that serve to accommodate the lattice mismatch across the interface. Despite variations in the thickness of the buffer layer between the two samples, we measured the average distance between the misfit dislocations, and we found no significant difference between the two samples. The average distance between the misfit dislocation in both samples is $d_{\text{misfit}} = (4.27 \pm 0.74)$ nm. Similar to the calculation of area dislocation density,³² the dislocation concentration ρ can be obtained using the following equation:

$$\rho = \frac{N - 1}{\sum_{i=1}^{N-1} L_{i,i+1}}, \quad (1)$$

where N represents the number of dislocations and $L_{i,i+1}$ denotes the distance between neighboring dislocations. Consequently, the misfit dislocation concentration is $\rho = (0.24 \pm 0.04)$ nm⁻¹.

In Fig. 3, NL-filtered HAADF images of the multilayer system are presented alongside their corresponding in-plane (ϵ_{xx}) and out-of-plane (ϵ_{yy}) strain maps derived from the GPA-analysis. These strain color maps provide a visualization of the strain distribution in each image. In both thick and thin samples, there are slight variations in the in-plane strain maps, while the out-of-plane strain maps for both samples indicate that the STF layers experience significant tensile strain relative to the LSC layers. Note that the reference area of the GPA-strain maps must be within the image (i.e., area with 0% strain). Due to the large overall thickness of the thick sample, multiple images had to be recorded to cover the whole film. Mean strain values, in Table I, for both samples are referenced to the bulk value of the LSC given in work by Rupp *et al.*,²⁴ that is, $a = 3.838$ Å. In the case of the thick sample [Fig. 3(a)], it is noteworthy that the last LSC-3 layer became amorphous during FIB sample preparation, rendering the GPA-analysis less meaningful on that layer. Additionally, layer overlap between

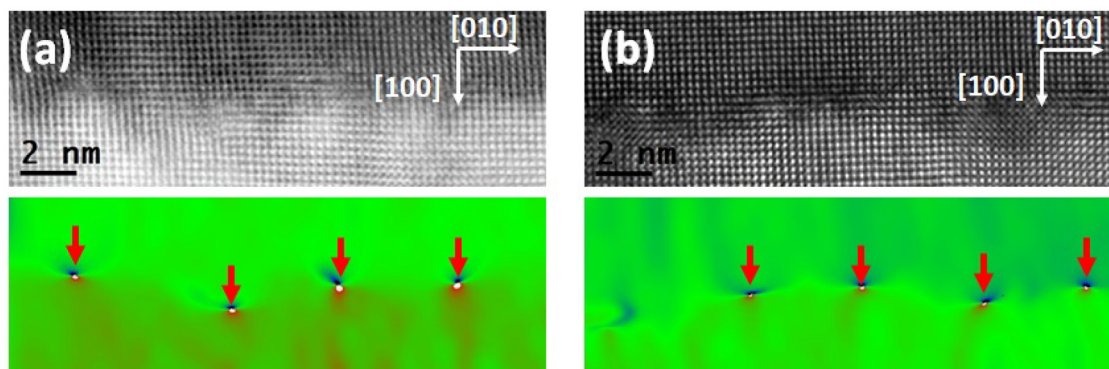


FIG. 2. NL-filtered HAADF images with their corresponding in-plane phase images for the thick (a) and thin (b) samples. Both images present the interface between the YSZ and GDC, while the red arrows denote misfit dislocations at the interface.

03 June 2025 08:16:09

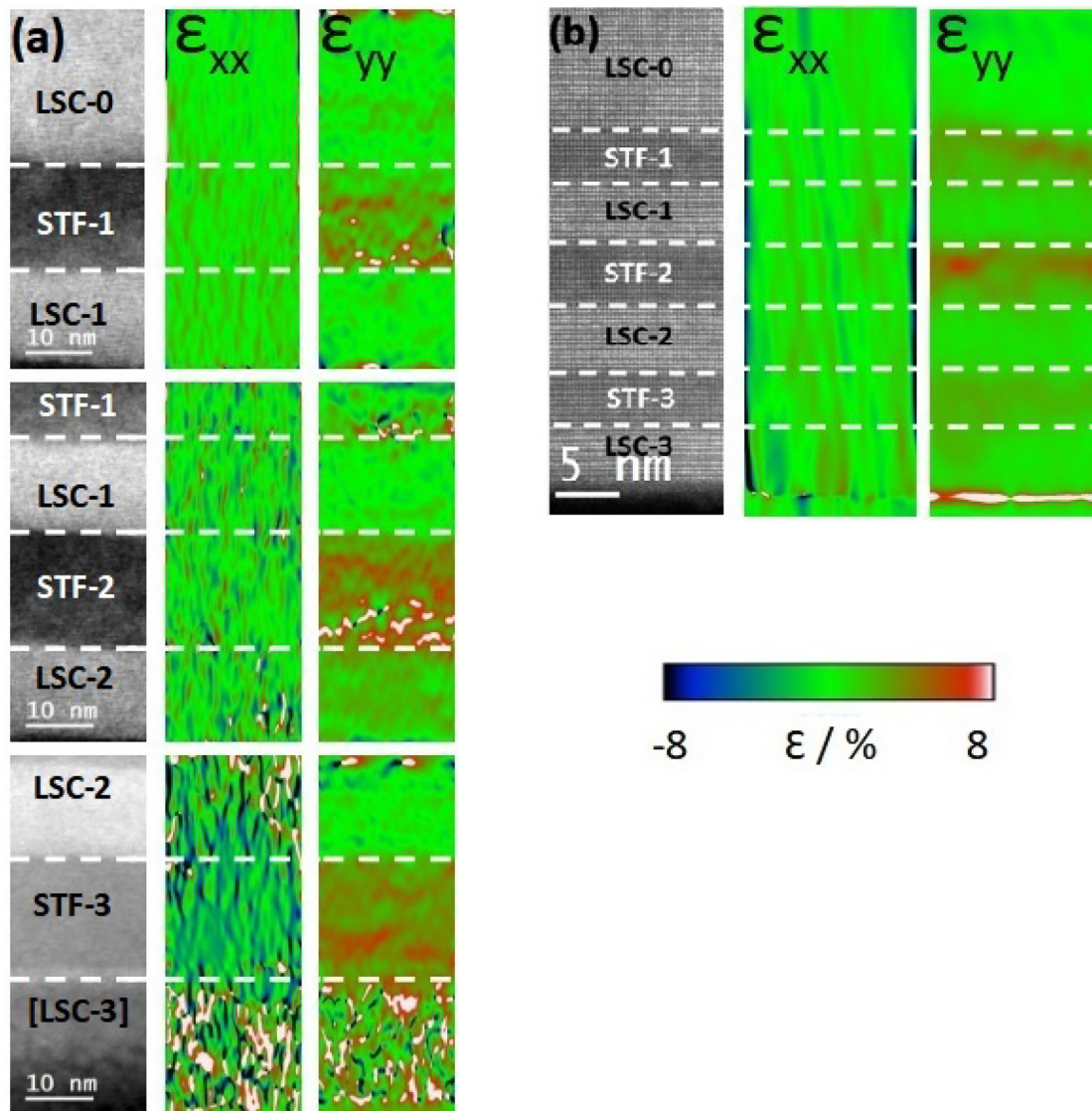


FIG. 3. NL-filtered HAADF images with their corresponding in-plane (ϵ_{xx}) and out-of-plane (ϵ_{yy}) strain maps for the thick sample (a) and for the thin sample (b).

images for the thick sample was crucial for calibration to ensure a meaningful strain relationship between different images. The process involves measuring the mean strain state of a layer in one image and then applying that value for the same layer in different images. Therefore, GPA maps in Fig. 3 do not show realistic strain evolution across the whole sample, but the calibrated values in Table I do.

From Table I, mean strain values of the samples show gradual in-plane strain evolution to the value of about 1.30% for the thick sample and about 1.20% for the thin sample. Due to the lateral geometrical constraints of the film growth, there must be a

mechanism for this relaxation to occur. Usually, this kind of relaxation is accompanied by misfit formation, similar to the case in Fig. 2. However, no regular misfit dislocations were found in either sample. In fact, the in-plane strain relaxation mechanism between the thick and thin samples is different, and it seems that these relaxation mechanisms do not depend on the multilayer system above but are simply two distinct ways to relax the in-plane strain. The thick sample experienced strain relaxation accompanied by an edge dislocation formation within the LSC-0 layer (for example, see Fig. 4). The thin sample also showed in-plane strain relaxation, but no edge dislocations were found. Instead, medium-magnification

TABLE I. Mean values of in-plane ϵ_{xx} and out-of-plane ϵ_{yy} strain states of each layer with respect to the bulk LSC $a = 3.838 \text{ \AA}$. Additionally, the values for the LSC-0 layer were assigned based on the results from the RMS measurements.

Layer	ϵ_{xx}^{Thick} (%)	ϵ_{yy}^{Thick} (%)	ϵ_{xx}^{Thin} (%)	ϵ_{yy}^{Thin} (%)
LSC-0	0.57	-1.00	0.57	-1.00
STF-1	1.17	1.35	0.96	2.24
LSC-1	1.33	-1.17	1.17	0.35
STF-2	1.32	2.68	1.23	2.33
LSC-2	1.31	0.59	1.20	0.27
STF-3	1.19	4.16	1.15	1.57
LSC-3	0.82	0.34

HAADF imaging (Fig. 5) reveals the process of this relaxation. The thin film forms amorphous phase regions in its structure which allows the lattice to expand in the lateral directions. This process of relaxation (i.e., amorphous phase formation) was not observed in the thick sample (see Fig. S2 in the [supplementary material](#)). The models of lattice expansion in the in-plane direction are presented in Fig. 6 for a thick sample (a) and for a thin sample (b). For the thick sample, edge dislocations allow the lattice to expand, while in the thin sample, the amorphous region (shown as a dotted region) allows the atomic planes to tilt inward slightly, leading to an increase in the lattice parameter.

In contrast, the out-of-plane strain relaxation does not require any mechanisms for the relaxation due to the fact that on the outer side is a vacuum, and the lattice can expand or contract freely. However, when the in-plane strain is applied, the material may adapt

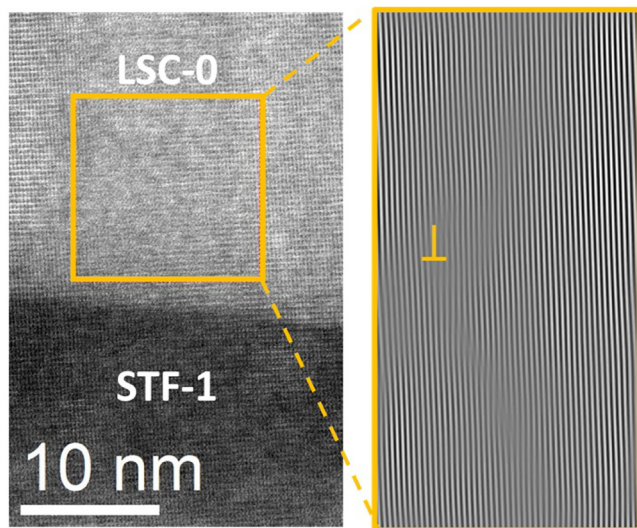


FIG. 4. NL-filtered HAADF image showing the area of LSC-0 and STF-1 layers of the thick sample. The inset shows Fourier transform of the filtered dimming spots (01-1) of the highlighted area in the LSC-0 layer, where the edge dislocation is indicated by a yellow “T”.

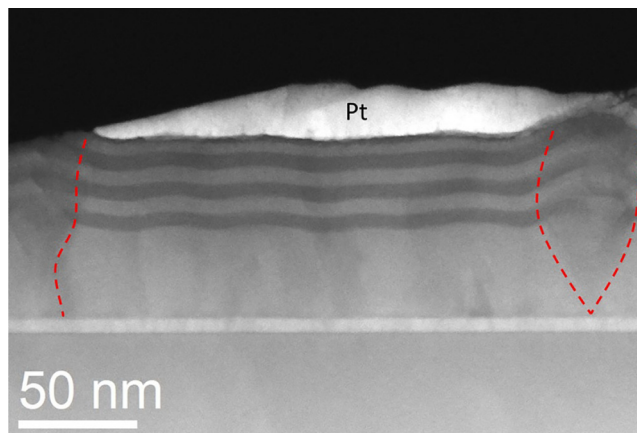


FIG. 5. Medium-magnification HAADF image showing the area of epitaxial film growth in-between the amorphous area highlighted by a red dashed line. The bright layer on top marked by Pt is the platinum protection layer deposited during the FIB-cut.

to it by automatically creating the out-of-plane strain (in the opposite direction), this phenomenon is known as Poisson’s effect.³³ For the thick sample, the out-of-plane distribution exhibits immediate change in the first STF-1 layer, while the LSC-1 layer seems to

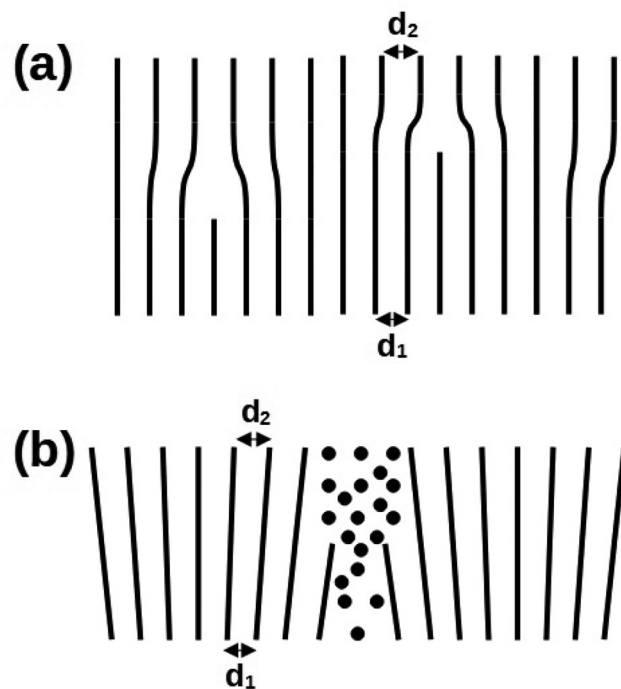


FIG. 6. Schematic models illustrating mechanisms of in-plane strain relaxation: (a) expansion through edge dislocations in a thick sample and (b) expansion via an amorphous (dotted) region in a thin sample.

03 June 2025 08:16:09

remain relatively unchanged. Subsequently, the evolution resumes in the STF-2 layer, with the LSC-2 layer also displaying significant strain change. Notably, the highest levels of strain change are observed in the STF-3 layer. In contrast to the thick sample, the thin sample demonstrates a distinctly different behavior. Out-of-plane strain change of the first STF-1 layer is even more pronounced than in the thick sample, while the first LSC-1 layer now exhibits strain, differing from the thick sample behavior. Furthermore, subsequent STF-2,3 layers also experience a strain change albeit the STF-3 has the smallest change of the three. As for the LSC-2,3 layers, their strain state is similar to that of LSC-1 layer.

Figure 7 presents reciprocal space mapping and line profiles of d-spacing evolution for both thick and thin multilayer samples. In (a) and (c), the reciprocal space maps for the thick and thin samples are shown, respectively, while (b) and (d) illustrate the out-of-plane d-spacing evolution obtained from GPA strain mapping. For the thick sample, noticeable elongation is observed in both STF and LSC reflections, indicating strain relaxation in the out-of-plane direction (q_z) for both structures. The mean lattice parameters derived from the STF reflection are $a_{\text{in-plane}} = 3.88 \text{ \AA}$ and $a_{\text{out-of-plane}} = 3.91 \text{ \AA}$, whereas for the LSC reflection, they are $a_{\text{in-plane}} = 3.86 \text{ \AA}$ and $a_{\text{out-of-plane}} = 3.80 \text{ \AA}$. Correspondingly, the line profile in Fig. 7(b) shows that the d-spacing of the LSC-0 layer is the smallest, with a slight increase for LSC-1 and even greater values for LSC-2. This continuous increase in d-spacing aligns well with the elongation observed in the reciprocal space maps, indicating a progressive change in lattice parameters across the layers.

Similarly, the STF-1,2,3 layers exhibit a continuous increase in d-spacing, reflecting the strain relaxation noted in the reciprocal space map. Continuous increase in d-spacing in a layer might indicate the presence of oxygen vacancy concentration gradient. More vacancies would cause the lattice parameter to expand because of Coulomb repulsion between the cations, coupled with the absence of an anion to screen this repulsion.¹⁰ In contrast, the thin sample displays a splitting of the LSC reflections in Fig. 7(c), where the higher intensity peak corresponds to the initial 35 nm LSC-0 layer, and the lower intensity peak represents the LSC-1,2,3 layers. The mean lattice parameters for the LSC-0 layer are $a_{\text{in-plane}} = 3.86 \text{ \AA}$ and $a_{\text{out-of-plane}} = 3.80 \text{ \AA}$, while for the LSC-1,2,3 layers, they are $a_{\text{in-plane}} = 3.89 \text{ \AA}$ and $a_{\text{out-of-plane}} = 3.85 \text{ \AA}$. The STF reflection shows mean lattice parameters of $a_{\text{in-plane}} = 3.89 \text{ \AA}$ and $a_{\text{out-of-plane}} = 3.91 \text{ \AA}$. The line profile in Fig. 7(d) reveals that the LSC-0 layer has the smallest out-of-plane d-spacing, while the LSC-1,2,3 layers exhibit larger d-spacing values, matching the peak split observed in the reciprocal space map. Interestingly, the thin sample's STF-1,2,3 layers show an increase in out-of-plane d-spacing in the middle of the film, followed by a decrease near the next LSC layer, as seen in Fig. 7(d). In contrast, the LSC-1,2,3 layers exhibit a slight reduction in the middle of the layer, followed by an increase as they approach the adjacent STF layer. This indicates that the STF layers adapt more significantly to the LSC layers near the interfaces rather than the other way around. However, this behavior is absent in the thick sample, where the out-of-plane d-spacing parameter steadily increases throughout the STF layers, as illustrated in Fig. 7(b).

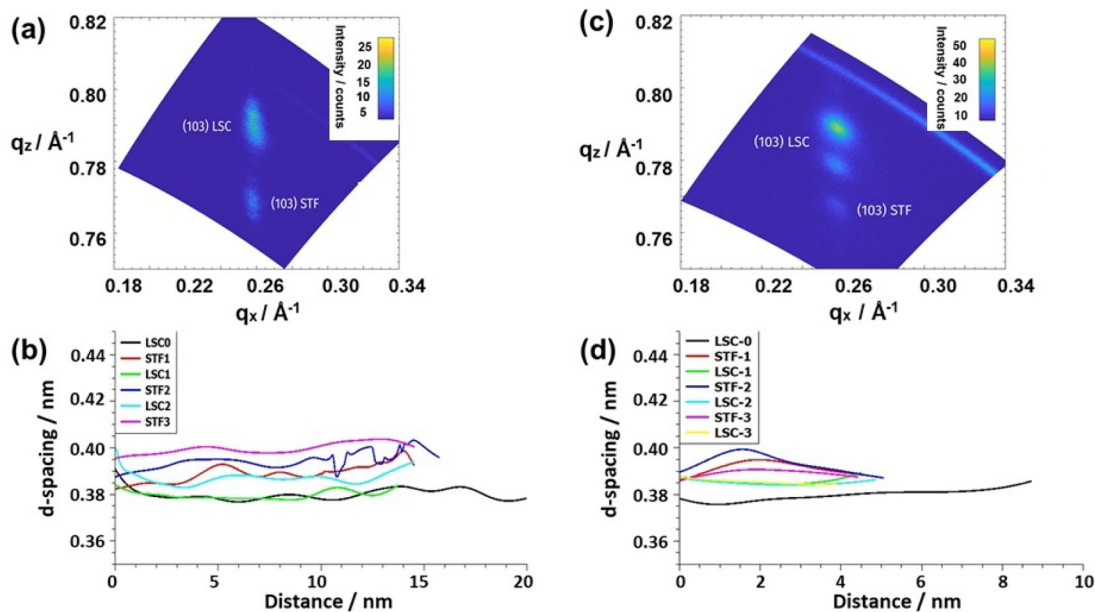


FIG. 7. (a) and (c) are reciprocal space mapping around 103 reflections for the thick sample and thin sample, respectively. (b) and (d) present d-spacing evolution, obtained from GPA-strain maps across the layers of the thick and thin samples, respectively. In (d), the evolution of the d-spacing is a continuous parameter because it was derived from a single GPA map [Fig. 3(b)]. In contrast, the d-spacing evolution in (a) is not a continuous parameter, as it was calculated from multiple GPA maps, as shown in Fig. 3(a).

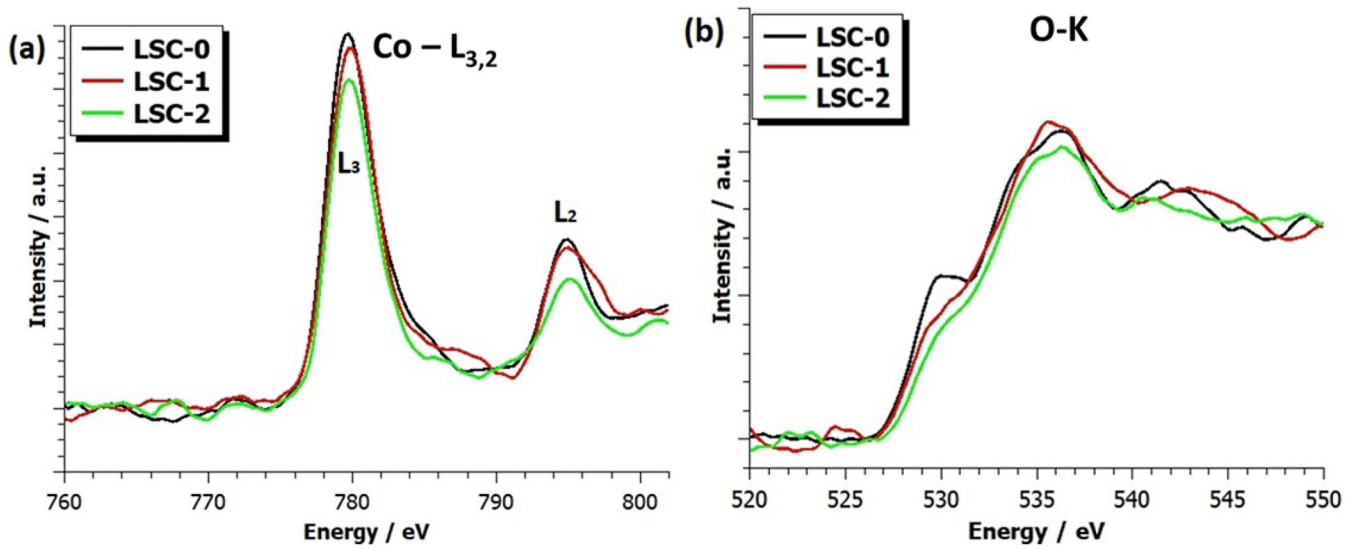


FIG. 8. EELS spectra of the thick sample showing Co L-edge (a) and O K-edge (b).

Chemical characterization was conducted using electron energy loss spectroscopy. In Figs. 8 and 9, the Co L-edge and O K-edge spectra of the LSC layers are presented for the thick and thin samples, respectively. Table II shows the values of the white line L_2/L_3 ratio calculated for the Co, Fe, and Ti transition metals. An increase in the white-line ratio indicates a decrease in the valence state of Co.^{29,34,35} Co white-line ratio of the thick sample shows that the LSC-1 stands out as a layer with the most oxygen content. However, it can be seen from the Co L-edge spectra that the Co- L_2

peak in the LSC-1 has been broadened. This unique and unexpected feature can be explained by the Coster-Kronig (CK) Auger decay effect. The Coster-Kronig (CK) Auger decay phenomenon involves the expulsion of an electron from the L shell of cobalt when subjected to an electron beam. The resulting vacancy is subsequently occupied by an electron from the higher energy L sub-shell. The surplus energy generated during the inner L-shell transition is further utilized to ionize the cobalt atom by ejecting an electron from the M shell. This process leads to the broadening

03 June 2025 08:16:09

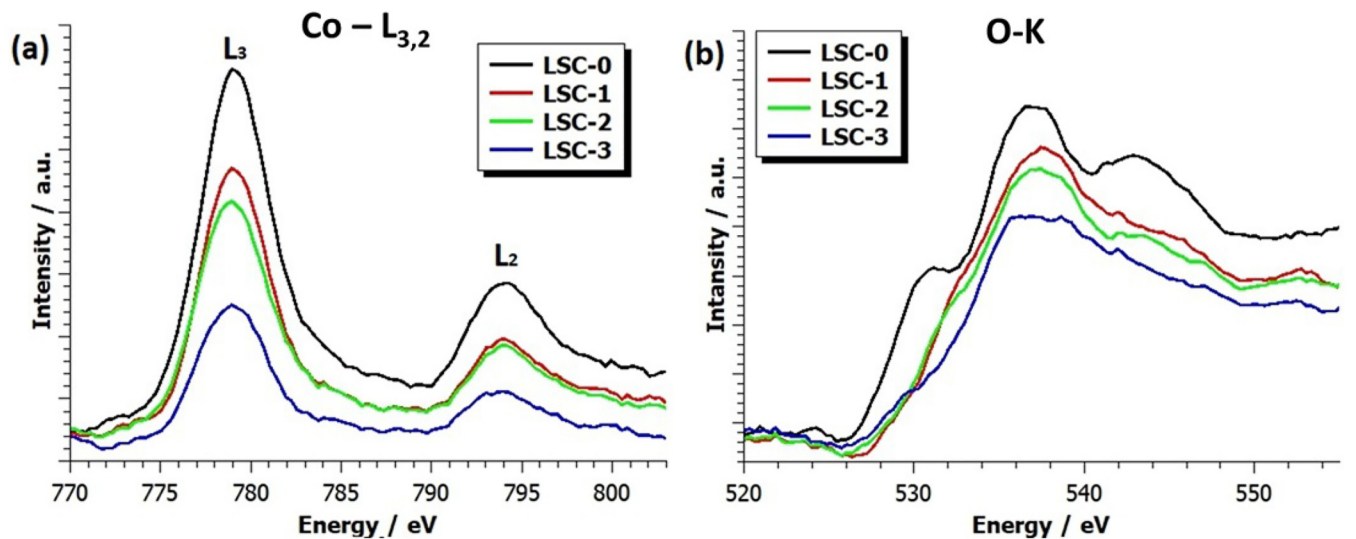


FIG. 9. EELS spectra of the thin sample showing Co L-edge (a) and O K-edge (b).

TABLE II. White-line ratio (I_{L_2}) of transition metals (Co, Fe, and Ti) in the individual layers of the system.

Layer	Co^{Thick}		Co^{Thin}	
LSC-0	2.53		2.14	
LSC-1	2.44		2.43	
LSC-2	2.61		2.46	
LSC-3	...		2.96	

Layer	Fe^{Thick}	Fe^{Thin}	Ti^{Thick}	Ti^{Thin}
STF-1	3.08	3.04	0.65	0.86
STF-2	3.13	3.11	0.67	0.87
STF-3	3.18	4.15	0.65	0.99

of the L_2 peak in transition metals, with cobalt exhibiting pronounced broadening as a notable consequence of the CK effect.^{10,36,37} As for the thin sample, the Co white-line ratio increases toward the surface. This suggests varying oxygen content among the layers and, consequently, that the oxygen vacancy concentration is the lowest in the LSC-0 layer and increases in the subsequent layers. Due to the CK-effect in the thick sample, rendering the white-line ratio characterization meaningless, the pre-peak integration was performed to probe the oxidation state of the layers. In the oxygen K-edges of both samples [refer to Figs. 8(b) and 9(b)], the oxygen pre-peak intensity is most pronounced in the LSC-0 layer. Oxygen pre-peak is suppressed in the LSC material with high oxygen vacancy concentration,^{35,38} hence further proving that the oxygen vacancy concentration is the lowest in the LSC-0 layer. Smaller, yet still noticeable oxygen pre-peak presence can be seen in the LSC-1,2,3 layers. Notably, the LSC-3 layer in the thin sample exhibits the smallest oxygen pre-peak. Oxygen pre-peak quantification was performed by the integration of the region of interest of

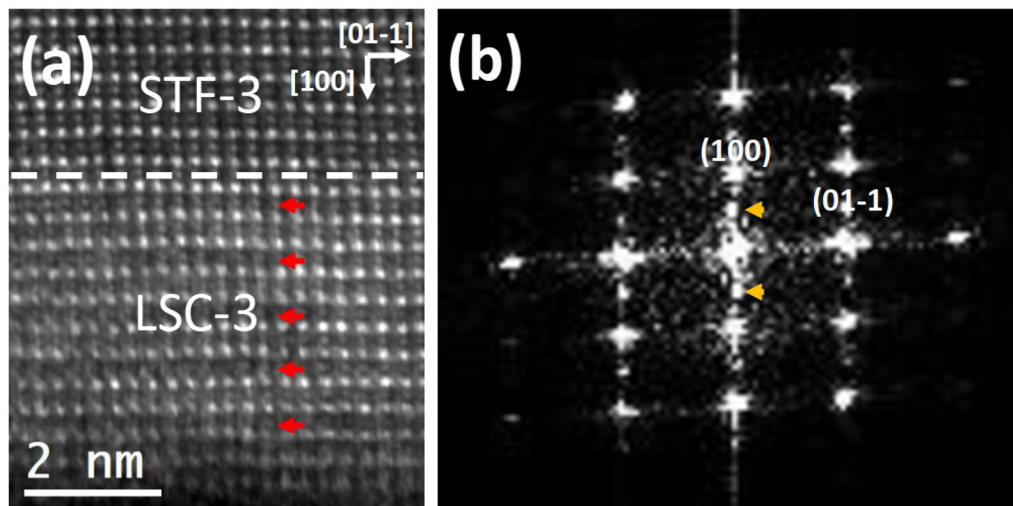
TABLE III. Oxygen pre-peak intensity obtained from intensity integration.

Layer	$I^{\text{Thick}}/\text{counts}$	$I^{\text{Thin}}/\text{counts}$
LSC-0	39 203	29 945 ± 1 297
LSC-1	31 858	26 503 ± 1 297
LSC-2	27 767	26 217 ± 1 297
LSC-3	...	18 091 ± 1 297

the spectrum intensity (see Figs. S3 and S4 in the [supplementary material](#)). Region of interest was set to the value of FWHM of the LSC-0 layer (2.70 eV for thin and 1.75 eV for thick samples). [Table III](#) shows oxygen pre-peak intensity obtained from intensity integration. In both samples, intensity is reduced toward the surface. With the highest Co white-line ratio observed and the smallest pre-peak intensity, we conclude that the oxidation state of the LSC-3 layer is the lowest among the layers analyzed.

For the STF layers, the white-line ratios of both Fe and Ti reveal that the oxygen vacancy concentration is notably different only in the STF-3 layer of the thin sample. Among all the STF layers, STF-3 of the thin sample exhibits the smallest d-spacing values, as shown in [Fig. 7\(d\)](#). This suggests that the variation in oxygen vacancy concentration is likely due to the material's accommodation to induced strain. The EELS spectra of the analyzed STF layers can be found in [Fig. S5](#) in the [supplementary material](#).

EELS analysis strongly suggests the presence of oxygen vacancies in the LSC-1,2,3 layers of the sample, with increasing concentration of vacancies toward the surface (i.e., most oxygen vacancies in the LSC-3). It has been shown that the oxygen vacancies in the LSC can be created in order to help the structure accommodate the strain imposed by various substrates. If the oxygen vacancy concentration is high enough, the perovskite structure may transition to brownmillerite via the ordering of these vacancies. [Figure 10\(a\)](#)

**FIG. 10.** (a) shows HAADF image with the LSC-3 layer in which the oxygen vacancies order in every other B-plane, as indicated by red arrows. (b) displays FFT of the image in which the half-integer reflections are highlighted by the yellow arrow.

shows this ordering in the LSC-3 layer of the thin sample. This layer is the only layer exhibiting this ordering among all the analyzed layers in both samples. This ordering further confirms the claim that the oxygen vacancy concentration is increasing toward the surface and is the highest in the last (LSC-3) layer. Although it is expected that the lattice parameter would expand with an increase in oxygen vacancy concentration, the expansion observed in Table I is not very pronounced. Therefore, we conclude that the relationship between oxygen vacancy concentration and lattice parameter is not straightforward.

IV. CONCLUSION

In this study, we investigated the phenomenon of local strain relaxation at multilayer heterointerfaces. Our findings reveal significant variations in strain dynamics across different layers. Despite both systems exhibiting epitaxial growth, the extent of strain relaxation varies notably. In a thinner sample, regions with an amorphous structure emerge due to changes in in-plane strain across the sample thickness, facilitating structural relaxation. Conversely, the thicker sample relaxed in-plane strain through the formation of edge dislocations. Additionally, the out-of-plane strain differs between samples, with thinner samples maintaining relatively constant values of strain across the layers, whereas strain relaxation in thicker samples increases toward the sample surface. White line ratios, obtained from EELS measurements, show that the first layer (LSC-0) of the thin sample has the highest content of oxygen atoms, while the results of the thick film are inconclusive due to the Coster-Kronig (CK) Auger decay phenomenon. However, the analysis of the pre-peak in the O K-edge reveals that the oxygen content of the LSC-0 layers is the highest in both samples.

SUPPLEMENTARY MATERIAL

See the [supplementary material](#) for a low-magnification HAADF image of the thick sample and the spectra used for oxygen pre-peak quantification in both samples. Additionally, the [supplementary material](#) includes Ti and Fe L-edge spectra used for white-line ratio quantification. Finally, a brief explanation of the procedure for determining the interface plane in the multilayer sample is also provided.

ACKNOWLEDGMENTS

We wish to acknowledge the financial support from the Austrian Science Fund (No. FWF P31654-N37) and the ESTEEM3 collaboration project. We wish to express our gratitude to Yong Huang for his help with FIB-polishing.

AUTHOR DECLARATIONS

Conflict of Interest

The authors have no conflicts to disclose.

Author Contributions

Sergej Ražnjević: Conceptualization (supporting); Formal analysis (lead); Investigation (lead); Software (lead); Writing – original draft (lead); Writing – review & editing (equal). **Sandra Drev:** Formal

analysis (supporting); Investigation (equal); Writing – review & editing (equal). **Andreas E. Bumberger:** Methodology (equal). **Matthäus Siebenhofer:** Conceptualization (supporting); Investigation (equal); Visualization (supporting); Writing – review & editing (equal). **Christin Böhme:** Conceptualization (supporting); Investigation (equal); Visualization (supporting); Writing – review & editing (equal). **Christoph Riedl:** Conceptualization (supporting); Visualization (supporting). **Jürgen Fleig:** Funding acquisition (equal); Supervision (supporting); Writing – review & editing (equal). **Miran Čeh:** Funding acquisition (equal); Supervision (supporting); Writing – review & editing (equal). **Markus Kubicek:** Conceptualization (equal); Funding acquisition (equal); Investigation (equal); Supervision (supporting); Writing – review & editing (equal). **Zaoli Zhang:** Conceptualization (equal); Formal analysis (equal); Funding acquisition (equal); Supervision (lead); Writing – review & editing (equal).

DATA AVAILABILITY

The data that support the findings of this study are available within the article and its [supplementary material](#).

REFERENCES

- ¹M. Laguna-Bercero, “Recent advances in high temperature electrolysis using solid oxide fuel cells: A review,” *J. Power Sources* **203**, 4–16 (2012).
- ²A. Akroot, “Effect of operating temperatures on the performance of a SOFC/GT hybrid system,” *Int. J. Trend Sci. Res. Develop.* **3**, 1512–1515 (2019).
- ³Q. Xu, Z. Guo, L. Xia, Q. He, Z. Li, I. T. Bello, K. Zheng, and M. Ni, “A comprehensive review of solid oxide fuel cells operating on various promising alternative fuels,” *Energy Convers. Manage.* **253**, 115175 (2022).
- ⁴M. Cimenti and J. M. Hill, “Direct utilization of liquid fuels in SOFC for portable applications: Challenges for the selection of alternative anodes,” *Energies* **2**, 377–410 (2009).
- ⁵K. Develos-Bagarinao, J. D. Vero, H. Kishimoto, T. Ishiyama, K. Yamaji, T. Horita, and H. Yokokawa, “Multilayered LSC and GDC: An approach for designing cathode materials with superior oxygen exchange properties for solid oxide fuel cells,” *Nano Energy* **52**, 369–380 (2018).
- ⁶A. Tarancon, “Strategies for lowering solid oxide fuel cells operating temperature,” *Energies* **2**, 1130–1150 (2009).
- ⁷S. Payán-Díaz, W. De La Cruz, R. Talamantes-Soto, A. Hurtado-Macías, and G. A. Hirata, “Effect of volume fraction on mechanical properties of Zr/ZrN multilayer systems,” *Ceram. Int.* **42**, 18806–18812 (2016).
- ⁸P. Zubko, S. Gariglio, M. Gabay, P. Ghosez, and J. Triscone, “Interface physics in complex oxide heterostructures,” *Annu. Rev. Condens. Matter Phys.* **2**, 141–165 (2011).
- ⁹J. Gazquez, S. Bose, M. Sharma, M. A. Torija, S. J. Pennycook, C. Leighton, and M. Varela, “Lattice mismatch accommodation via oxygen vacancy ordering in epitaxial $\text{La}_{0.5}\text{Sr}_{0.5}\text{CoO}_{3-\delta}$ thin films,” *APL Mater.* **1**, 012105 (2013).
- ¹⁰S. Ražnjević, M. Siebenhofer, A. E. Bumberger, C. Böhme, C. Riedl, Z. Chen, M. Kubicek, and Z. Zhang, “Electron beam-induced brownmillerite–perovskite phase transition in $\text{La}_{0.6}\text{Sr}_{0.4}\text{CoO}_{3-\delta}$,” *Appl. Phys. Lett.* **122**, 211903 (2023).
- ¹¹Y. P. Ivanov, M. Kubicek, M. Siebenhofer, A. Viernstein, H. Hutter, J. Fleig, A. Chuvilin, and Z. Zhang, “Strain-induced structure and oxygen transport interactions in epitaxial $\text{La}_{0.6}\text{Sr}_{0.4}\text{CoO}_{3-\delta}$,” *Commun. Mater.* **1**, 25 (2020).
- ¹²G. H. Jonker and J. H. V. Santen, “Magnetic compounds with perovskite structure III. Ferromagnetic compounds of cobalt,” *Physica* **19**, 120–130 (1953).
- ¹³H. Taguchi, M. Shimada, and M. Koizumi, “The effect of oxygen vacancies on the magnetic properties in the system $\text{SrCoO}_{3-\delta}$ ($0 \leq \delta < 0.5$),” *J. Solid State Chem.* **29**, 221–225 (1979).

- ¹⁴Z. Cai, M. Kubicek, J. Fleig, and B. Yildiz, "Chemical heterogeneities on $\text{La}_{0.6}\text{Sr}_{0.4}\text{CoO}_{3-\delta}$ thin films—correlations to cathode surface activity and stability," *Chem. Mater.* **24**, 1116–1127 (2012).
- ¹⁵S. B. Adler, "Factors governing oxygen reduction in solid oxide fuel cell cathodes," *Chem. Rev.* **104**, 4791–4844 (2004).
- ¹⁶A. N. Petrov, O. F. Kononchuk, A. V. Andreev, V. A. Cherepanov, and P. Kofstad, "Crystal structure, electrical and magnetic properties of $\text{La}_{1-x}\text{Sr}_x\text{CoO}_{3-y}$," *Solid State Ionics* **80**, 189–199 (1995).
- ¹⁷H. Yokokawa, N. Sakai, T. Horita, K. Yamaji, and M. E. Brito, "Electrolytes for solid-oxide fuel cells," *MRS Bull.* **30**, 591–595 (2005).
- ¹⁸A. J. Jacobson, "Materials for solid oxide fuel cells," *Chem. Mater.* **22**, 660–674 (2010).
- ¹⁹C. substrates, see <https://www.crystalsubstrates.com/products/strontium-titanate-rtio3-substrates> for "Strontium Titanate (STO) SrTiO_3 " (2024); accessed 14 February 2024.
- ²⁰J. Kubacki, D. Kajewski, J. Goraus, K. Szot, A. Koehl, C. Lenser, R. Dittmann, and J. Szade, "Impact of Fe doping on the electronic structure of SrTiO_3 thin films determined by resonant photoemission," *J. Chem. Phys.* **148**, 154702 (2018).
- ²¹L. F. da Silva, M. I. B. Bernardi, L. J. Q. Maia, G. J. M. Frigo, and V. R. Mastelaro, "Synthesis and thermal decomposition of $\text{SrTi}_{1-x}\text{Fe}_x\text{O}_3$ ($0.0 \leq x \leq 0.1$) powders obtained by the polymeric precursor method," *J. Therm. Anal. Calorim.* **97**, 173–177 (2009).
- ²²L. F. da Silva, J. M'Peko, J. Andrés, A. Beltrán, L. Gracia, M. I. B. Bernardi, A. Mesquita, E. Antonelli, M. L. Moreira, and V. R. Mastelaro, "Insight into the effects of Fe addition on the local structure and electronic properties of SrTiO_3 ," *J. Phys. Chem. C* **118**, 4930–4940 (2014).
- ²³S. Zhang, H. Wang, M. Y. Lu, A. Zhang, L. Mogni, Q. Liu, C. Li, C. Li, and S. Barnett, "Cobalt-substituted $\text{SrTi}_{0.3}\text{Fe}_{0.7}\text{O}_{3-\delta}$: A stable high-performance oxygen electrode material for intermediate-temperature solid oxide electrochemical cells," *Energy Environ. Sci.* **11**, 1870–1879 (2018).
- ²⁴G. M. Rupp, A. Schmid, A. Nanning, and J. Fleig, "The superior properties of $\text{La}_{0.6}\text{Ba}_{0.4}\text{CoO}_{3-\delta}$ thin film electrodes for oxygen exchange in comparison to $\text{La}_{0.6}\text{Sr}_{0.4}\text{CoO}_{3-\delta}$," *J. Electrochem. Soc.* **163**, F564–F573 (2016).
- ²⁵H. Du, "A nonlinear filtering algorithm for denoising HR(S)TEM micrographs," *Ultramicroscopy* **151**, 62–67 (2015).
- ²⁶H. Du, "Gpa: Geometric phase analysis software," available at <https://er-c.org/index.php/software/stem-data-analysis/gpa/> (2018).
- ²⁷D. H. Pearson, B. Fultz, and C. C. Ahn, "Measurements of 3D state occupancy in transition metals using electron energy loss spectrometry," *Appl. Phys. Lett.* **53**, 1405–1407 (1988).
- ²⁸D. H. Pearson, C. C. Ahn, and B. Fultz, "White lines and d-electron occupancies for the 3d and 4d transition metals," *Phys. Rev. B* **47**, 8471–8478 (1993).
- ²⁹Z. L. Wang, J. S. Yin, and Y. D. Jiang, "EELS analysis of cation valence states and oxygen vacancies in magnetic oxides," *Micron* **31**, 571–580 (2000).
- ³⁰T. Riedl, T. Gemming, and K. Wetzig, "Extraction of EELS white-line intensities of manganese compounds: Methods, accuracy, and valence sensitivity," *Ultramicroscopy* **106**, 284–291 (2006).
- ³¹E. J. Crumlin, S. Ahn, D. Lee, E. Mutoro, M. D. Biegalski, H. M. Christen, and Y. Shao-Horn, "Oxygen electrocatalysis on epitaxial $\text{La}_{0.6}\text{Sr}_{0.4}\text{CoO}_{3-\delta}$ perovskite thin films for solid oxide fuel cells," *J. Electrochem. Soc.* **159**, F219 (2012).
- ³²X. Gu, Z. Zhang, M. Bartosik, P. H. Mayrhofer, and H. Duan, "Dislocation densities and alternating strain fields in CrN/AlN nanolayers," *Thin Solid Films* **638**, 189–200 (2017).
- ³³H. Gercek, "Poisson's ratio values for rocks," *Int. J. Rock Mech. Min. Sci.* **44**, 1–13 (2007).
- ³⁴S. Stemmer, A. Sane, N. D. Browning, and T. J. Mazanec, "Characterization of oxygen-deficient $\text{SrCoO}_{3-\delta}$ by electron energy-loss spectroscopy and z-contrast imaging," *Solid State Ionics* **130**, 71–80 (2000).
- ³⁵N. Biskup, J. Salafranca, V. Mehta, M. P. Oxley, Y. Suzuki, S. J. Pennycook, S. T. Pantelides, and M. Varela, "Insulating ferromagnetic $\text{LaCoO}_{3-\delta}$ films: A phase induced by ordering of oxygen vacancies," *Phys. Rev. Lett.* **112**, 087202 (2014).
- ³⁶R. Nyholm, N. Martensson, A. Lebugle, and U. Axelsson, "Auger and Coster-Kronig broadening effects in the 2p and 3p photoelectron spectra from the metals ^{22}Ti – ^{30}Zn ," *J. Phys. F: Metal Phys.* **11**, 1727–33 (1981).
- ³⁷Y. Liao, see <https://www.globalsino.com/EM/> for "Practical Electron Microscopy and Database" (2006).
- ³⁸J. Gazquez, W. Luo, M. P. Oxley, M. Prange, M. A. Torija, M. Sharma, C. Leighton, S. T. Pantelides, S. J. Pennycook, and M. Varela, "Atomic-resolution imaging of spin-state superlattices in nanopockets within cobaltite thin films," *Nano Lett.* **11**, 973–976 (2011).